Topographic Coupling of Surface and Internal Kelvin Waves

SHENN-YU CHAO[1]

Research and Data Systems, Inc., Lanham, MD 20801

(Manuscript received 8 August 1979, in final form 3 March 1980)

ABSTRACT

An analytical method is developed to compute the diffraction of a barotropic Kelvin wave by a localized topographic irregularity on an otherwise flat-bottom ocean with an arbitrary vertical stratification. The bump topography is assumed to be small in height compared to the water depth of the flat-bottom ocean. It is found that all baroclinic mode Kelvin waves will be generated downstream of the bump, with the first baroclinic mode having the largest amplitude. At subinertial frequencies ($\omega < f$) localized disturbances are also generated with higher vertical modes trapped nearer to the bump. At superinertial frequencies ($\omega > f$) cylindrical Poincaré waves with certain anisotropy are generated at ($x = x_0$, $y = 0$) and ($x = -x_0$, $y = 0$), where (x_0,0) is the center of the bump topography, and the y axis is the coastline. The Poincaré waves favor the lowest few modes, with the baroclinic modes having stronger tendencies to be directionally anisotropic. The baroclinic Poincaré waves radiating offshore from the bump topography could contribute to the internal wave field in the open ocean and provide an alternative mechanism to dissipate the barotropic tides. Order-of-magnitude estimates show that an energy flux of ~0.09 W per centimeter coastline could be converted from the M2 tide in the eastern Pacific.

1. Introduction

In recent years there has been considerable work on the effects of coastal irregularities on the propagation of the barotropic tides, modeled by Kelvin and Poincaré waves. These studies are best summarized by LeBlond and Mysak (1978). Buchwald (1968) employed the Wiener-Hopf technique to study the diffracted wave field due to a Kelvin wave incident on a right-angle corner. At subinertial frequencies ($\omega < f$) he showed that a Kelvin wave propagated around the corner without loss in amplitude, while at higher frequencies ($\omega > f$) the amplitude of the incident wave was reduced and anisotropic cylindrical Poincaré waves were generated at the corner. It should be noted, however, that a much more general method was developed earlier by Williams (1959) to study problems concerning the diffraction of electromagnetic waves by wedges. Using Williams' technique, Packham and Williams (1968) showed that Buchwald's conclusions held for bends of all other angles except $\pi/(2n + 1)$, $n = 1, 2 \ldots$, in which case the superinertial Kelvin wave propagated around the corner without a reduction in amplitude. A similar result was obtained by Roseau (1967) using a different integral transform method. Miles (1972) further obtained the phase of the transmission coefficient of the diffracted Kelvin wave field.

The diffraction of a Kelvin wave by small coastal and topographic irregularities on an otherwise rectilinear coast was studied by Pinsent (1972). Howe and Mysak (1973) and Mysak and Tang (1974) also dealt with extensive irregular coastlines by treating small irregularities as a stationary, random zero-mean function.

All of the results described above were barotropic free Kelvin waves. Moreover, all the studies other than that of Pinsent were concerned with coastal irregularities. Although their results can easily be transformed into the case of a single baroclinic mode, the problems concerning the coupling of barotropic and baroclinic modes of Kelvin waves by topography were not addressed. The aspect of energy transfer from the barotropic to the baroclinic components of the Kelvin wave is of interest, since for all practical purposes the transferred energy is lost from the surface Kelvin wave (in particular, the surface tide) and effectively represents its dissipation. In this respect studies were concentrated on the case of normal incidence of tides onto a continental slope (Rattray, 1960; Cox and Sandstrom, 1962; Baines, 1974; Sandstrom, 1976). While their models may be used to account for a large portion of tidal dissipation of the world ocean, it is also true that propagation appears longshore in some area (e.g., eastern North Pacific Ocean) in the form of Kelvin waves (Platzman, 1979). This provides us with the incentive to study the diffraction of a barotropic Kelvin wave by a

[1] Present affiliation: Ocean Sciences Center, Nova University, Dania, FL 33004.

0022-3670/80/081147-12$07.00

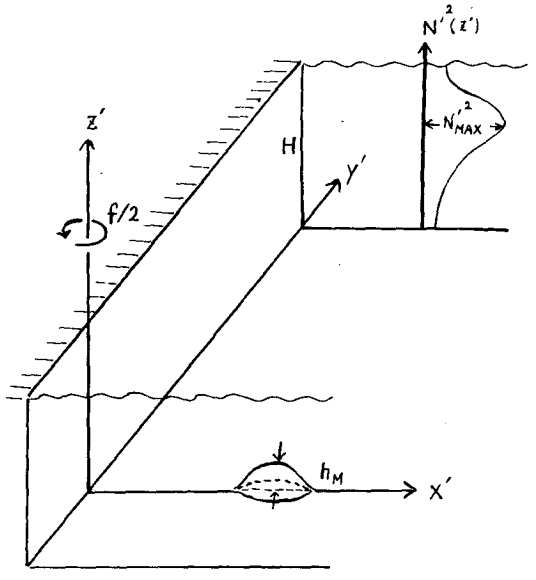

FIG. 1. The geometry of the hydrodynamic system.

localized topographic irregularity in a stably stratified coastal ocean. To focus our attention to the mesoscale phenomenon, our scope is confined to the bump size on the order of the baroclinic Rossby radius of deformation [i.e., O(100 km)]. Fig. 1 shows the geometry of the hydrodynamic system.

Conceivably, the impingement of a barotropic Kelvin wave on a localized bump will generate baroclinic mode Kelvin waves in the forward direction. For $\omega > f$, Poincaré waves will also be generated in the form of two-dimensional cylindrical waves, which may contribute to the internal wave field in the open ocean. Nevertheless, the quantitative behavior of the diffracted wave fields was not addressed in the previous literature. It is of note here that the effects of a small longshore topography on the wind-forced and free internal Kelvin waves were addressed by Killworth (1978), in which ultralow-frequency ($\omega \ll f$) waves in a linearly stratified ocean were considered.

Section 2 will be devoted to the formulation of the problem. In Section 3 the analytical solution will be developed by employing a normal mode decomposition in the vertical direction, a Fourier transform in the longshore direction, and Green's function technique (Chao *et al.*, 1979; Chao and Janowitz, 1979) in the onshore-offshore direction. Asymptotic solutions away from the topography for a delta-function bump and an extended bump case are obtained explicitly. An order-of-magnitude estimate of energy transfer from barotropic to baroclinic modes is given in Section 4. Results and conclusions are briefly summarized in Section 5.

2. Formulation

We consider a model coastal hydrodynamic system with continuous density stratification and a localized topographic irregularity $h'(x',y')$ superimposed on an otherwise flat-bottom ocean floor ($z' = 0$). The linearized, inviscid, f-plane equation for the conservation of potential vorticity in terms of the pressure field follows (Wang and Mooers, 1976), i.e.,

$$\left(\frac{\partial^2}{\partial x'^2} + \frac{\partial^2}{\partial y'^2}\right)p' + \left(\frac{\partial^2}{\partial t'^2} + f^2\right)\frac{\partial}{\partial z'}\left(\frac{1}{N'^2(z')}\frac{\partial}{\partial z'}p'\right) = 0, \quad (1)$$

where x' is positive offshore, y' longshore northward, z' vertically upward, and $N'^2(z')$ is the square of the local Brunt-Väisälä frequency (see Fig. 1).

We nondimensionalize the variables z' by the depth of the ocean H, t' by f^{-1}, N' by $N_{\max}$, (x',y') by the internal Rossby radius of deformation ($\mathrm{Ri} = N_{\max}H/f$), and bump topography h' by its maximum height h_M. Assuming a monochromatic wave solution $P'(x,y,z,t) = P(x,y,z)e^{-i\omega t}$, the nondimensional governing equation becomes

$$\left(\frac{\partial^2}{\partial x^2} + \frac{\partial^2}{\partial y^2}\right)P + (1 - \omega^2)\frac{\partial}{\partial z}\left(\frac{1}{N^2}\frac{\partial}{\partial z}P\right) = 0. \quad (2)$$

For a deep ocean ($H \sim 4$ km) at latitude 30°N, the onshore/offshore scale of the barotropic Kelvin wave is the external Rossby radius of deformation ($R_e = (gH)^{1/2}/f \approx 2700$ km), which is a substantial fraction of the width of a typical ocean basin. The internal Rossby radius of deformation (R_i) is on the order of 100 km, which is very small compared to R_e. In scaling (x',y') by R_i, we have implicitly assumed that the topography-induced response is predominantly baroclinic. This is, in fact, the case for a bump size of O(100 km), as we will see later in the next section.

The boundary conditions associated with Eq. (2) are as follows:

1. No normal flow at the coast, or

$$x = 0, \quad P_x + \frac{i}{\omega}P_y = 0. \quad (3)$$

2. The disturbance vanishes far offshore, or

$$x \to \infty, \quad P \to 0. \quad (4)$$

3. Free surface condition at the top, i.e.,

$$z = 1, \quad P_z + S^2N^2(1)P = 0. \quad (5)$$

4. No normal flow at the bottom, i.e.,

$$z = \epsilon h(x,y),$$

$$P_z = \frac{N^2}{1-\omega^2}\left[\left(P_x + \frac{i}{\omega}P_y\right)\epsilon h_x + \left(P_y - \frac{i}{\omega}P_x\right)\epsilon h_y\right]. \quad (6)$$

Here $\epsilon = h_M/H$ is assumed to be small compared to 1, and the stratification parameter S is defined as R_i/R_e, which is a very small parameter. For $\omega < 1$, the boundary condition 4 specifies a coastally trapped disturbance. For $\omega > 1$, Eqs. (2) and (4) give us a radiation condition, in which cylindrical Poincaré waves are outgoing as $x \to \infty$. In addition to boundary conditions (3)–(6), appropriate radiation conditions as $|y| \to \infty$ also must be specified to make the problem well posed.

We now expand the regular perturbation (i.e., Born's approximation) in a power series of ϵ, i.e.,

$$P = P_0(x,y,z) + \epsilon P^*(x,y,z) + O(\epsilon^2). \quad (7)$$

It follows that $P_0(x,y,z)$ satisfies the same governing Eq. (2) and boundary conditions (3)–(5), except that the boundary condition (6) is replaced by a homogeneous one, i.e.,

$$P_{0z} = 0, \quad z = 0. \quad (8)$$

The factor $(1 - \omega^2)$ in the denominator of Eq. (6) will not cause a breakdown of our perturbation as $\omega \to 1$, because velocity components (u,v) in the (x,y) directions, which are inversely proportional to $(1 - \omega^2)$, are supposed to be well-defined quantities. The zeroth-order solution is assumed to be a free, barotropic mode Kelvin wave traveling in the $-y$ direction, with pressure field defined as

$$P_0(x,y,z) = A(z)\exp(-\lambda_0^{1/2}x - i\omega\lambda_0^{1/2}y), \quad (9)$$

where $A(z)$ [$\approx A(0) \equiv 1$] is the vertical structure modified by stratification, and $\lambda_0^{1/2} \sim O(S)$ is the barotropic (lowest) mode eigenvalue of the vertical decomposition (LeBlond and Mysak, 1978). In dimensional form $\lambda_0^{1/2} \approx (gH)^{-1/2}$ which is the inverse of the phase speed of barotropic Kelvin waves modified by the stratification. A brief account of vertical normal mode decomposition will be given in the next section.

To $O(\epsilon)$, the wave diffracted field by the topographic irregularity $P^*(x,y,z)$ is governed by the same set of Eqs. (2)–(5), except that the bottom boundary condition (6) is replaced by an inhomogeneous one, i.e.,

$$z = 0, \quad P_z^* = \frac{iN^2}{\omega}\lambda_0^{1/2}P_0(x,y,0)h_y. \quad (10)$$

For convenience, we will drop the asterisk from now on with the understanding that P represents the diffracted wave field.

3. Analytical solution

Before the vertical modal decomposition can be carried out, we first define the vertical normal modes $G_n(z)$ as the normalized eigenfunction of the following equation:

$$\frac{d}{dz}\left(\frac{1}{N^2(z)}\frac{d}{dz}G_n\right) + \lambda_n G_n = 0, \quad (11)$$

where λ_n is the eigenvalue of Eq. (11) subjected to the boundary conditions

$$\left.\begin{aligned} z = 0, \quad & dG_n/dz = 0 \\ z = 1, \quad & dG_n/dz + S^2N^2(1)G_n = 0 \end{aligned}\right\}. \quad (12)$$

The G_n's are normalized such that

$$\int_0^1 G_n^2(z)dz = 1 \quad (13)$$

for all $n \geq 0$.

We now carry out the vertical decomposition as follows. First we multiply Eq. (2) by $G_n(z)$ and integrate vertically from $z = 0$ to $z = 1$. After twice integrating the last term on the left-hand side of Eq. (2) by parts, and utilizing the boundary conditions (5), (10) and (13), it follows that

$$\left(\frac{\partial^2}{\partial x^2} + \frac{\partial^2}{\partial y^2}\right)P_n + \lambda_n(\omega^2 - 1)P_n = \frac{i(1-\omega^2)}{\omega} \times \lambda_0^{1/2}G_n(0)h_y\exp(-\lambda_0^{1/2}x - i\omega\lambda_0^{1/2}y) \quad (14)$$

along with the boundary conditions

$$\left.\begin{aligned} x = 0, \quad & P_{nx} + \frac{i}{\omega}P_{ny} = 0 \\ x \to \infty, \quad & P_n \to 0 \end{aligned}\right\}. \quad (15)$$

The P_n's are defined such that

$$P(x,y,z) = \sum_{n=0}^{\infty} P_n(x,y)G_n(z). \quad (16)$$

Eq. (14), along with the boundary conditions (15), can now be solved by applying a Fourier transform in the longshore direction:

$$\begin{Bmatrix} \phi(k,x) \\ S_n(k,x) \end{Bmatrix} = \frac{1}{\sqrt{2\pi}}\int_{-\infty}^{+\infty} e^{iky}\begin{Bmatrix} P_n(x,y) \\ R_n(x,y) \end{Bmatrix}dy, \quad (17)$$

where $R_n(x,y)$ is the inhomogeneous term in (14). It follows that

$$\phi_{nxx} - [k^2 - (\omega^2 - 1)\lambda_n]\phi_n = S_n(k,x), \quad (18)$$

where ϕ_n satisfies the same boundary conditions as

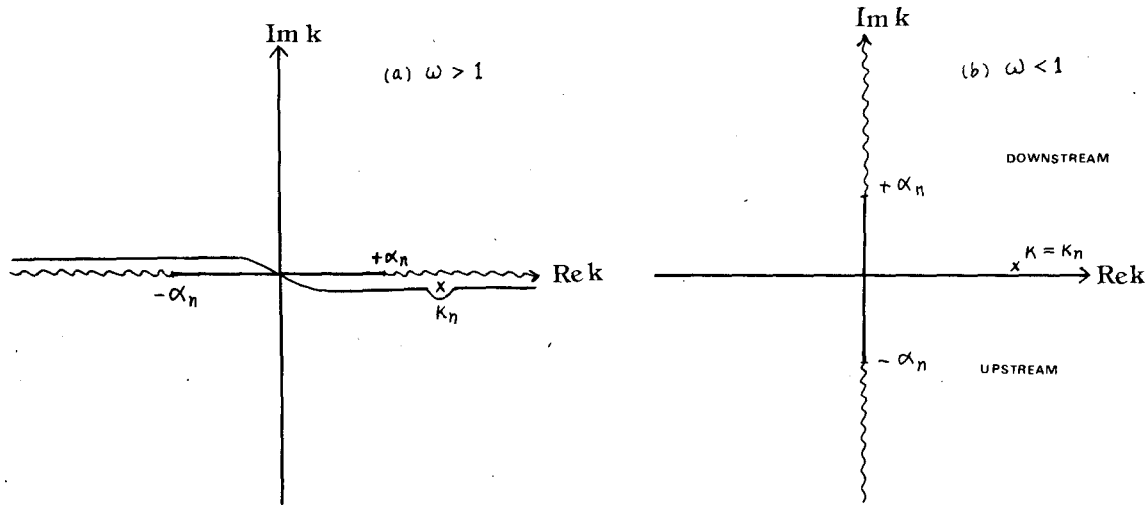

FIG. 2. Diagram of branch cuts and poles in the complex k-plane for (a) $\omega > 1$ and (b) $\omega < 1$, respectively. The contours of integrations are also shown.

P_n in Eq. (15). Eq. (18) can readily be solved in terms of the Green's function technique (Chao and Janowitz, 1979). We first define a Green's function $G_n(x,\zeta,k)$ such that

$$\phi_n(k,x) = \int_0^\infty G_n(x,\zeta,k)S_n(k,\zeta)d\zeta. \tag{19}$$

The Green's function $G(x,\zeta,k)$ is defined as

$$G(x,\zeta,k) = \frac{\phi_{n1}(x_<)\phi_{n2}(x_>)}{D(k)}, \tag{20}$$

where $x_<$ ($x_>$) is the smaller (larger) between x and ζ. The functions ϕ_{n1}, ϕ_{n2} are homogeneous solutions of Eq. (18), with ϕ_{n1} satisfying the boundary condition at $z = 0$, and ϕ_{n2} satisfying the boundary condition as $x \to \infty$. The function $D(k)$ is the Wronskian of Eq. (18), defined as

$$D(k) = \phi_{n1}\phi_{n2_x} - \phi_{n2}\phi_{n1_x}. \tag{21}$$

The formal solution of $P_n(x,y)$ can be expressed as

$$P_n(x,y) = \frac{1}{\sqrt{2\pi}} \int_{-\infty}^{+\infty} e^{-iky} \times \int_0^\infty G_n(x,\zeta,k)S_n(k,\zeta)d\zeta dk. \tag{22}$$

It is straightforward to find ϕ_{n1} as

$$\phi_{n1} = \frac{(k^2 - \alpha_n^2)^{1/2} - k/\omega}{(k^2 - \alpha_n^2)^{1/2} + k/\omega} \exp[(k^2 - \alpha_n^2)^{1/2}x] + \exp[-(k^2 - \alpha_n^2)^{1/2}x] \tag{23}$$

and ϕ_{n2} as

$$\phi_{n2} = \exp[-(k^2 - \alpha_n^2)^{1/2}x], \tag{24}$$

where $\alpha_n \equiv [\lambda_n(\omega^2 - 1)]^{1/2}$. The Wronskian $D(k)$ can also be computed from (21) as

$$D(k) = \frac{2[k/\omega - (k^2 - \alpha_n^2)^{1/2}]}{(k^2 - \alpha_n^2)^{1/2} + k/\omega}(k^2 - \alpha_n^2)^{1/2}. \tag{25}$$

It is seen that the singularities in the integration of (22) in the complex k-plane consist of a simple pole at $k = k_n = \omega\lambda_n^{1/2}$ and two branch points at $k = \pm\alpha_n$. The pole at $k = \omega\lambda_n^{1/2}$ satisfies the dispersion relation of the nth baroclinic mode Kelvin wave. In compliance with the radiation condition, we include a small friction parameter σ such that $\omega = \omega_0 + i\sigma$. It then follows that a small positive imaginary part has to be added to α_n and k_n. The singularities and branch cuts in the complex k-plane as $\sigma \to 0$ for $\omega > 1$ and $\omega < 1$ are illustrated in Fig. 2. For $\omega > 1$, the branch cuts are defined from $k = \alpha_n$ to $k \to +\infty$ and from $k = -\alpha_n$ to $k \to -\infty$ such that $(k^2 - \alpha_n^2)^{1/2} \to |k|$ as $k \to \pm\infty$, while for $\omega < 1$, α_n is positive imaginary, the branch cuts are defined from $k = \alpha_n$ to $k \to +i\infty$ and from $k = -\alpha_n$ to $k \to -i\infty$, and the branch is illustrated in Fig. 2b.

Regrouping the integrand of Eq. (22) by using (23) and (24), it follows that

$$P_n(x,y) = \frac{-1}{2\sqrt{2\pi}} \int_0^\infty d\zeta \int_{-\infty}^{+\infty} e^{-iky} \times \frac{S_n(k,\zeta)}{(k^2 - \alpha_n^2)^{1/2}} \left\{ \exp[-(k^2 - \alpha_n^2)^{1/2}(x_> - x_<)] + \frac{(k^2 - \alpha_n^2)^{1/2} + k/\omega}{(k^2 - \alpha_n^2)^{1/2} - k/\omega} \times \exp[-(k^2 - \alpha_n^2)^{1/2}(x_> + x_<)] \right\} dk. \tag{26}$$

We next consider a change of variable by means of which (26) can be considered from a more general point of view (see, e.g., Noble, 1958). We first consider the case that $\omega > 1$. For simplicity suppose that $\sigma \to 0$ and α_n is then real and positive. The transformation $k = -\alpha_n \cos\beta$, where $k = k_R + ik_I$ and $\beta = \mu + i\nu$, transforms the complex k-plane cut along the real axis from $-\infty$ to $-\alpha_n$ and from $+\alpha_n$ to $+\infty$ into the region $0 \leq \mu \leq \pi$, $-\infty < \nu < \infty$ in the β-plane. We have then

$$\left.\begin{aligned} k &= -\alpha_n \cos\beta \\ (k^2 - \alpha_n^2)^{1/2} &= -i\alpha_n \sin\beta \end{aligned}\right\}, \tag{27}$$

and therefore the change of variable $k = -\alpha_n \cos\beta$ in the integral (26) gives

$$\begin{aligned} P_n(x,y) = \frac{-i}{2\sqrt{2\pi}} \int_0^{+\infty} d\zeta \int_\Gamma S_n(-\alpha_n \cos\beta, \zeta) \\ \times \left\{ \exp[i\alpha_n r_1 \cos(\beta - \theta_1)] \right. \\ \left. + \frac{-\cos\beta - i\omega \sin\beta}{\cos\beta - i\omega \sin\beta} \right. \\ \left. \times \exp[i\alpha_n r_2 \cos(\beta - \theta_2)] \right\} d\beta, \end{aligned} \tag{28}$$

where Γ is the contour of integration in the β-plane as shown in Fig. 3, and where

$$\left.\begin{aligned} r_1 &= [(x_> - x_<)^2 + y^2]^{1/2}, \quad \tan\theta_1 = \frac{x_> - x_<}{y} \\ r_2 &= [(x_> + x_<)^2 + y^2]^{1/2}, \quad \tan\theta_2 = \frac{x_> + x_<}{y} \end{aligned}\right\}. \tag{29}$$

Eqs. (28) and (29) give the formal solution of the posed problem.

To simplify the analysis, it is conceptually useful to consider first a delta-function bump of the form

$$h(x,y) = V_b \delta(x - x_0)\delta(y), \tag{30}$$

where V_b is the volume of the bump. In other words, we keep the volume of the bump fixed but shrink the size of the bump to zero. Although the delta-function bump introduced will make our normal mode expansion divergent, as we will see later, it provides some basic properties of the solution. Also, the delta-function solution can be easily integrated to obtain results for complicated and extensive bump topographies.

Using Eqs. (14), (17) and (30), the inhomogeneous term in (18), i.e., $S_n(k,x)$, can be computed as

$$\begin{aligned} S_n(k,x) = \frac{V_b}{\sqrt{2\pi}} \frac{1 - \omega^2}{\omega} (k - \omega\sqrt{\lambda_0}) \\ \times \sqrt{\lambda_0} G_n(0) \exp(-\lambda_0^{1/2} x)\delta(x - x_0) \end{aligned} \tag{31}$$

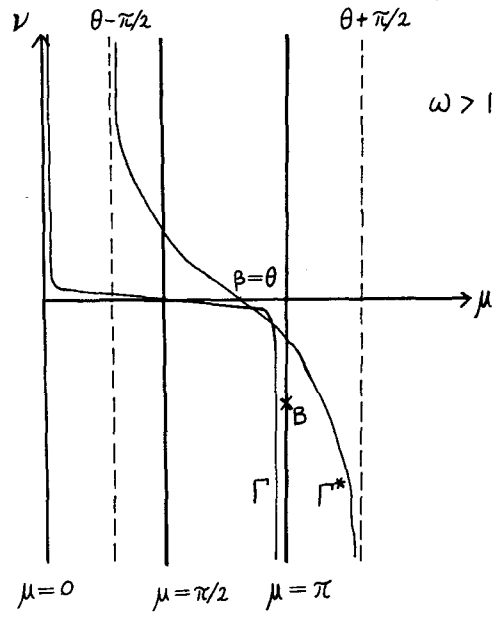

FIG. 3. Image of Fig. 2a in the complex β-plane, under the transformation $k = -\alpha_n \cos\beta$ for $\omega > 1$. Γ is the image of the original contour of integration. Γ^* is the path of steepest descent passing through $\beta = \theta$.

and the double integrals in (28) can be reduced to a single integration:

$$\begin{aligned} P_n(x,y) = \frac{+iV_b}{4\pi} \frac{\omega^2 - 1}{\omega} \sqrt{\lambda_0} G_n(0) \exp(-\lambda_0^{1/2} x_0) \\ \times \int_\Gamma (\alpha_n \cos\beta + \omega\lambda_0^{1/2}) \\ \times \left\{ \exp[i\alpha_n r_1 \cos(\beta - \theta_1)] \right. \\ \left. - \frac{\cos\beta + i\omega \sin\beta}{\cos\beta - i\omega \sin\beta} \right. \\ \left. \times \exp[i\alpha_n r_2 \cos(\beta - \theta_2)] \right\} d\beta, \end{aligned} \tag{32}$$

where $x_>$ ($x_<$) in (29) is the larger (smaller) between x and x_0.

Eq. (32) is the complete solution for the delta-function bump. A general idea of the nature of the diffracted waves may be obtained by considering the asymptotic form of $P_n(x,y)$ for large r_1 and r_2. This can be accomplished by the method of steepest descent (for details see Noble, 1958; Buchwald, 1968). We notice that the transformed exponents in the braces of (32) have saddle points at

$$\beta = \theta_1, \quad \beta = \theta_2$$

for the first and second term, respectively. The path of steepest descent makes an angle of 135° with the

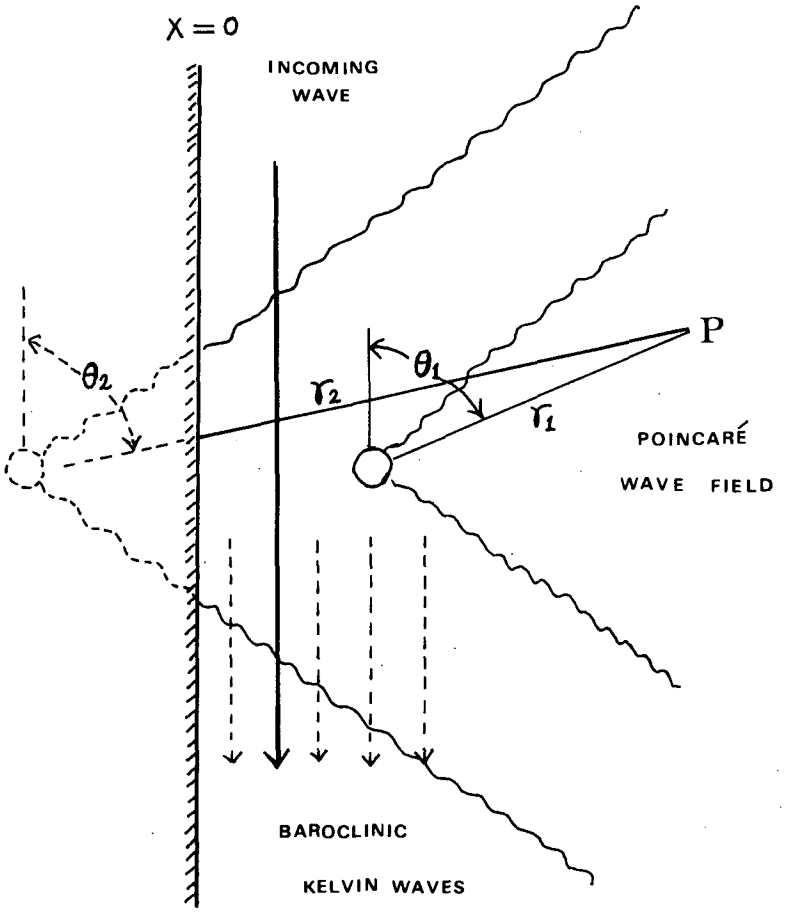

FIG. 4. Illustration of the physical process of diffraction by a localized topographic irregularity.

μ axis, while the asymptotes of the path of steepest descent are the lines $\mu = \theta_{1,2} \pm \pi/2$, so that the path of steepest descent passing through $\beta = \theta_{1,2}$ has the form of Γ^* in Fig. 3. The contribution from the saddle points in (32) is then

$$\tilde{P}_n(x,y) \approx \frac{+iV_b}{4}\frac{\omega^2-1}{\omega}\lambda_0^{1/2}G_n(0)\exp(-\lambda_0^{1/2}x_0) \times \left\{(\alpha_n\cos\theta_1 + \omega\lambda_0^{1/2})H_0^{(1)}(\alpha_n r_1) - (\alpha_n\cos\theta_2 + \omega\lambda_0^{1/2}) \times \frac{\cos\theta_2 + i\omega\sin\theta_2}{\cos\theta_2 - i\omega\sin\theta_2}H_0^{(1)}(\alpha_n r_2)\right\}, \quad (33)$$

where $H_0^{(1)}$ is the Hankel function of the first kind.

Notice that a pole at B [$\beta = \pi - i\cosh^{-1}(k_n/\alpha_n)$], which corresponds to $k = k_n = \omega\sqrt{\lambda_n}$ in the complex k-plane, exists in the second integrand of (32) and represents an nth mode diffracted Kelvin wave. When $0 \leq \theta_2 \leq \theta^* = \pi/2 + \cos^{-1}[(\omega^2-1)/\omega^2]^{1/2}$ the contour Γ can be deformed into Γ^* without capturing the pole. As θ_2 increases from θ^*, the pole at B will be captured, so that the contribution from the residue at point B must be taken into consideration. The nth transmitted baroclinic Kelvin wave is then

$$P_n^w(x,y) = \{+i\omega V_b\lambda_0^{1/2}G_n(0)(\lambda_n^{1/2} - \lambda_0^{1/2}) \times \exp[-(\lambda_0^{1/2} + \lambda_n^{1/2})x_0]\} \times \exp(-\lambda_n^{1/2}x - i\omega\lambda_n^{1/2}y), \quad (34)$$

where the term in braces gives the amplitude of the transmitted wave.

The physical explanation for the results in (33) and (34) is simple. The $P_n^w(x,y)$ is a Kelvin wave generated by the bump. One can see from (34) that the topographic irregularity does not generate barotropic Kelvin waves, i.e., $P_{n=0}^w = 0$. For $x_0 > 0$, the series $\sum_{n=1}^{\infty} P_n^w G_n(z)$ converges absolutely. On the other hand, $\tilde{P}_n(x,y)$ consists of two outgoing cylindrical Poincaré waves radiating from $(x_0, 0)$ and $(-x_0, 0)$, respectively, and traveling with a phase speed ω/α_n. It is also of note here that

$$H_0^{(1)}(\alpha_n r) \sim (\alpha_n r)^{-1/2}\exp(i\alpha_n r),$$

for

$$r = r_{1,2} \gg 1 \tag{35}$$

is isotropic. The factors associated with $H_0^{(1)}(\alpha_n r_1)$ and $H_0^{(1)}(\alpha_n r_2)$ in (33) represent the anisotropy of Poincaré waves. Fig. 4 illustrates the physical features associated with the asymptotic solution.

The computation for the case $\omega < 1$ is very much the same as above. In this case α_n is positive imaginary, the transformation (27) maps the k-plane, cut as in Fig. 2b, on to the strip $0 < \mu < \pi$, illustrated in Fig. 5. The contour Γ coincide with the line $\mu = \pi/2$. The saddle point is at $\mu = \theta$ as before and the path of steepest descent Γ^* is parallel to the imaginary axis. It can easily be shown that the contribution from the saddle point is

$$\tilde{P}_n(x,y) \sim f_1(\theta_1) r_1^{-1/2} \exp(-|\alpha_n| r) + f_2(\theta_2) r_2^{-1/2} \exp(-|\alpha_n| r_2), \tag{36}$$

which is localized near the bump topography, with higher modes trapped closer to the bump. The diffracted baroclinic Kelvin wave is still represented by Eq. (34) for $\omega < 1$, and is captured as $\theta \geq \pi/2$.

As we mentioned earlier, the diffracted Poincaré wave fields in (33) are anisotropic in the θ_1 and θ_2 directions. One can see from (33) that the factor

$$\frac{\cos\theta_2 + i\omega \sin\theta_2}{\cos\theta_2 - i\omega \sin\theta_2}$$

in $H_0^{(1)}(\alpha_n r_2)$ represents only a phase shift of the diffracted Poincaré waves, while the factor $(\alpha_n \cos\theta_{1,2} + \omega\sqrt{\lambda_0})$ gives the polarization in the amplitudes of waves. The two Poincaré waves $H_0^{(1)}(\alpha_n r_1)$ and $H_0^{(1)}(\alpha_n r_2)$ reach the maximum amplitudes as $\theta_{1,2} \to 0$ and zero amplitude (i.e., the nodal line) as

$$\theta_{1,2} = \cos\left(-\frac{\omega\sqrt{\lambda_0}}{\alpha_n}\right) = \cos\left[-\left(\frac{\lambda_0}{\lambda_n}\frac{\omega^2}{\omega^2 - 1}\right)^{1/2}\right]. \tag{37}$$

Thus, the scattering of the Poincaré waves favors the backward direction ($y \to +\infty$) for a delta-function bump, consistent with the barotropic model of Howe and Mysak (1973).

The forward-scattered amplitudes of baroclinic Kelvin waves are also of interest. To $O(\epsilon)$, the amplitude of each baroclinic mode Kelvin wave is linearly proportional to the frequency (ω) and volume of the bump (V_b). For $x_0 > 0$, the series

$$\sum_{n=1}^{\infty} P_n^w(x,y) G_n(z)$$

converges absolutely and is thus amenable for numerical computation. If $x_0 = 0$, the series diverges and our approach fails to give a uniformly valid result. Of course, if $x_0 = 0$ the Green's function technique developed in this section is not applicable in the first place.

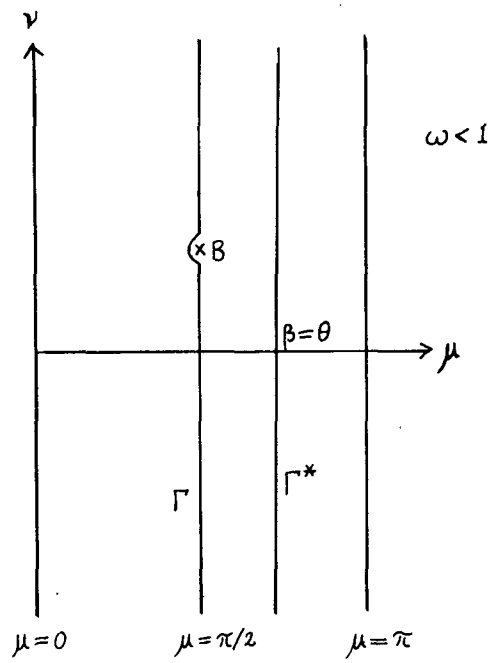

FIG. 5. Image of Fig. 2b in the complex β-plane under the transformation $k = -i|\alpha_n| \cos\beta$ for $\omega < 1$. Γ^* is the path of steepest descent.

The question as to which baroclinic mode is dominant can be answered as follows. In the simple case with N^2 = constant, the boundary value problem (11)–(13) can be cast into a simple equation in which the vertical normal modes can be expressed in terms of trigonometry functions. For a typical ocean $N'^2 \sim 10^{-5}$ s^{-1}, $H \sim 4$ km, S^2 is typically as small as 10^{-3}, and the internal Rossby radius of deformation is ~120 km. Therefore all vertical modes other than the barotropic one can be computed by assuming a rigid-lid at the surface, i.e.,

$$dG_n/dz = 0, \quad z = 1 \quad \text{for} \quad n \geq 1. \tag{38}$$

It follows that

$$\lambda_0 \approx S^2, \quad \lambda_n \approx n^2\pi^2 (n \geq 1) \tag{39}$$

and the eigenfunctions are

$$G_0 \approx 1, \quad G_n(z) \approx \sqrt{2} \cos n\pi z (n \geq 1). \tag{40}$$

From Eq. (40) it also follows that $G_n(0) \approx \sqrt{2}$ for all $n \geq 1$. Therefore, for a bump of volume V_b localized at $x = x_0$, the factor

$$g(\lambda_n^{1/2}) = (\lambda_n^{1/2} - \lambda_0^{1/2}) \times \exp[-(\lambda_0^{1/2} + \lambda_n^{1/2})x_0] \tag{41}$$

in Eq. (34) determines the amplitude of each baro-

clinic mode. If we treat $g(\lambda_n^{1/2})$ as a continuous function of $\lambda_n^{1/2}$, it can be seen easily that $g(\lambda_n^{1/2})$ has only one maximum at

$$\lambda_n^{1/2} = x_0^{-1} + \lambda_0^{1/2}. \tag{42}$$

Since $\lambda_n^{1/2}$ is a discrete set of numbers, we conclude that the mth baroclinic mode with $\lambda_m^{1/2}$ closest to $x_0^{-1} + \lambda_0^{1/2}$ has the maximum amplitude. For $x_0 \geq 0.3$, $x_0^{-1} + \lambda_0^{1/2} \leq 3.1$, while $\lambda_1^{1/2} \sim \pi$, it is thus concluded that for all practical cases ($x_0 \geq 0.3$, say), the first baroclinic mode has the largest amplitude.

One defect of the above result is that the Poincaré wave field is not a convergent series, because in (33), $\tilde{P}_n \propto \alpha_n^{1/2}$, so that $\sum_{n=0}^{\infty} \tilde{P}_n(x,y)G_n(z)$ does not converge. This is, of course, an artifact of the delta-function solution. A realistic bump has to be introduced to eliminate the divergence. As an example, we next consider a bump of the form

$$h(x,y) = e^{-a^2y^2}q(x), \tag{43}$$

where $q(x)$ is centered at $x = x_0 \geq 1/4a$ and is defined as

$$q(x) = \begin{cases} \cos[2a\pi(x - x_0)], \\ \qquad x_0 - 1/4a \leq x \leq x_0 + 1/4a \\ 0, \qquad \text{otherwise.} \end{cases} \tag{44}$$

The horizontal dimension of the bump topography is inversely proportional to a in this case. We notice that, in carrying out the perturbation of Eq. (6), $h_y \sim$ O(1) was implicitly assumed. Therefore, following Eq. (43), it is required that $a \sim$ O(1) [bump size $\sim$ O(100 km)]. It also follows from (17) that

$$S_n(k,x) = \frac{1}{\sqrt{2}a}\frac{1-\omega^2}{\omega}\lambda_0^{1/2}G_n(0)(k - \omega\lambda_0^{1/2}) \times \exp[-\lambda_0^{1/2}x - (k^2 - \omega\lambda_0^{1/2})^2/4a^2]q(x). \tag{45}$$

The Poincaré waves can be obtained from (38) and (45), i.e.,

$$\tilde{P}_n(x,y) = \frac{i\pi^{3/2}(\omega^2-1)}{\omega}\lambda_0^{1/2}G_n(0)\exp(-\lambda_0^{1/2}x_0)\Bigg[(\alpha_n\cos\theta_1 + \omega\lambda_0^{1/2}) \times \frac{\exp[-(\alpha_n\cos\theta_1 + \omega\lambda_0^{1/2})^2/4a^2]}{(\lambda_0^{1/2} + i\alpha_n\sin\theta_1)^2 + 4a^2\pi^2}\cosh[(\lambda_0^{1/2} + i\alpha_n\sin\theta_1)/4a]H_0^{(1)}(\alpha_n r_1) - \frac{\cos\theta_2 + i\omega\sin\theta_2}{\cos\theta_2 - i\omega\sin\theta_2} \times \exp[-(\alpha_n\cos\theta_2 + \omega\lambda_0^{1/2})^2/4a^2]\frac{(\alpha_n\cos\theta_2 + \omega\lambda_0^{1/2})\cosh[(\lambda_0^{1/2} - i\alpha_n\sin\theta_2)/4a]}{(\lambda_0^{1/2} - i\alpha_n\sin\theta_2)^2 + 4a^2\pi^2}H_0^{(1)}(\alpha_n r_2)\Bigg],$$

for

$$x > x_0 + 1/4a; \quad r_1, r_2 \gg 1/\alpha_n. \tag{46}$$

which is easily seen to form a convergent series with the lowest few modes having the largest amplitudes.

The dependence of the amplitude of scattered Poincaré waves on x_0 is determined by the exponential $\exp(-\lambda_0^{1/2}x_0)$, which is proportional to the amplitude of the incoming Kelvin wave at $x = x_0$. Two Poincaré waves are still originated at $(x_0, 0)$ and $(-x_0, 0)$ as in the case of delta-function bump. The angular dependence of the amplitudes of Poincaré waves is, however, sensitive to the size of the bump. The factor $(\cos\theta_2 + i\omega\sin\theta_2)/(\cos\theta_2 - i\omega\sin\theta_2)$ affects only the phase of waves, hence the amplitudes of Poincaré waves $H_0^{(1)}(\alpha_n r_1)$ and $H_0^{(1)}(\alpha_n r_2)$ have the same angular dependence on θ_1 and θ_2, respectively. Since $\lambda_0^{1/2}$ is smaller than $\lambda_n^{1/2}$ ($n \geq 1$) by a factor of 100 or more, the cases for barotropic and baroclinic Poincaré waves have to be considered separately.

a. Barotropic Poincaré waves ($n = 0$)

In this case $\alpha_0 = [\lambda_0(\omega^2 - 1)]^{1/2}$ is smaller than $\omega\lambda_0^{1/2}$, so that there is no nodal line for $0 \leq \theta \leq \pi$. The basic features of the angular dependence of barotropic Poincaré waves can be obtained as follows. Since $\alpha_0 \sim \lambda_0^{1/2} \ll 1$, it follows that

$$\exp\left[-\left(\frac{\alpha_0\cos\theta + \omega\lambda_0^{1/2}}{2a}\right)^2\right] \sim \left|\cosh[(\lambda_0^{1/2} + i\alpha_0\sin\theta)/4a]\right| \approx 1$$

for a mesoscale bump [$a \sim$ O(1)]. The amplitudes of Poincaré waves are only sensitive to the factor $(\alpha_0\cos\theta + \omega\lambda_0^{1/2})$, which is maximum as $\theta = \theta_{1,2} \to 0$ and decreases slowly as θ increases from 0 to π. Therefore, the scattering of Poincaré waves favors the upstream direction, as is the case of a delta-function bump.

b. Baroclinic Poincaré waves ($n \geq 1$)

In this case since $\lambda_n^{1/2} \gg \lambda_0^{1/2}$, thus $\alpha_n = [\lambda_n(\omega^2 - 1)]^{1/2}$ is usually much larger than $\omega\lambda_0^{1/2}$ unless $\omega \to 1$. Therefore a nodal line at $\tilde{\theta} = 90° + \cos^{-1}(\omega\lambda_0^{1/2}/\alpha_n)$ exists between 0 and π unless $\omega \to 1$. The angular dependence of baroclinic Poincaré waves is distinctly different from the barotropic case. For $\alpha_n \gg 2a$, the amplitudes of Poincaré waves are essentially determined by the exponential

$$\exp[-(\alpha_n\cos\theta + \omega\lambda_0^{1/2})^2/4a^2]$$

which has its maximum at $\cos\theta = 0$ or $\theta = \pi/2$. Notice that the nodal line $\theta = \tilde{\theta}$ is also very near

$\theta = \pi/2$. Therefore a two-peak structure approximately symmetric with respect to $\tilde{\theta}$ is expected in this case. For $\alpha_n < 2a$, the amplitudes of internal Poincaré waves are more sensitive to the factor $(\alpha_n \cos\theta + \omega\lambda_0^{1/2})$, which has its maxima at $\theta = 0$ and π, with a nodal line at $\tilde{\theta}$.

Fig. 6 shows the anisotropy of Poincaré waves for three different sizes of the bump, as represented by the factor

$$A = \left| \frac{(\alpha_n \cos\theta + \omega\lambda_0^{1/2}) \cosh[(\lambda_0^{1/2} \pm i\alpha_n \sin\theta/4a]}{(\lambda_0^{1/2} \pm i\alpha_n \sin\theta)^2 + 4a^2\pi^2} \times \exp[-(\alpha_n \cos\theta + \omega\lambda_0^{1/2})^2/4a^2] \right|$$

in Eq. (46). The frequency ω is fixed at 1.5. In Fig. 6a we choose $a = 0.3$, which corresponds to a bump size of 200 km for a baroclinic Rossby radius of deformation $R_i = 120$ km. In this case the barotropic Poincaré wave dominates except near $\theta = 82°$, 102° where the first baroclinic mode dominates. The barotropic Poincaré wave favors the backscattering direction as expected (Howe and Mysak, 1973). Modes higher than $n = 1$ are too small compared to the first baroclinic mode and can be neglected completely. In Fig. 6b $a = 1$ corresponds to a bump scale of 60 km. The amplitude of the barotropic Poincaré wave is reduced by a factor of 10 compared to the previous case $a = 0.3$ (Fig. 6a). Higher baroclinic modes are becoming more important compared to the first baroclinic mode, which is the dominant modal response. All of the baroclinic modes are approximately symmetric with respect to their nodal lines at $\tilde{\theta} = 90° + \cos^{-1}(\omega\lambda_0^{1/2}/\alpha_n)$. In Fig. 6c a is further increased to 2.5, which corresponds to a bump size of 25 km. In this case the barotropic response can be neglected completely. The first baroclinic mode dominates over higher modes only in the upstream and downstream directions ($\theta \to 0, \pi$). Higher baroclinic modes are becoming increasingly important as a increases. Thus a large (small) size bump tends to generate lower (higher) modal response. As the size of the bump is reduced to zero (i.e., delta-function bump), the vertical modal expansion diverges for the Poincaré wave fields.

The diffracted Kelvin waves generated by the extended bump topography defined in (43) can also be computed easily, i.e.,

$$P_n^w(x,y) = +4i\omega\pi^{3/2}\lambda_0^{1/2}G_n(0)(\lambda_n^{1/2} - \lambda_0^{1/2}) \times \exp[-(\lambda_0^{1/2} + \lambda_n^{1/2})x_0] \times \frac{\cosh[(\lambda_n^{1/2} + \lambda_0^{1/2})/4a]}{(\lambda_n^{1/2} + \lambda_0^{1/2})^2 + 4a^2\pi^2} \times \exp\{-[\omega^2(\lambda_n^{1/2} - \lambda_0^{1/2})^2]/4a^2\} \times \exp(-\lambda_n^{1/2}x - i\omega\lambda_n^{1/2}y). \quad (47)$$

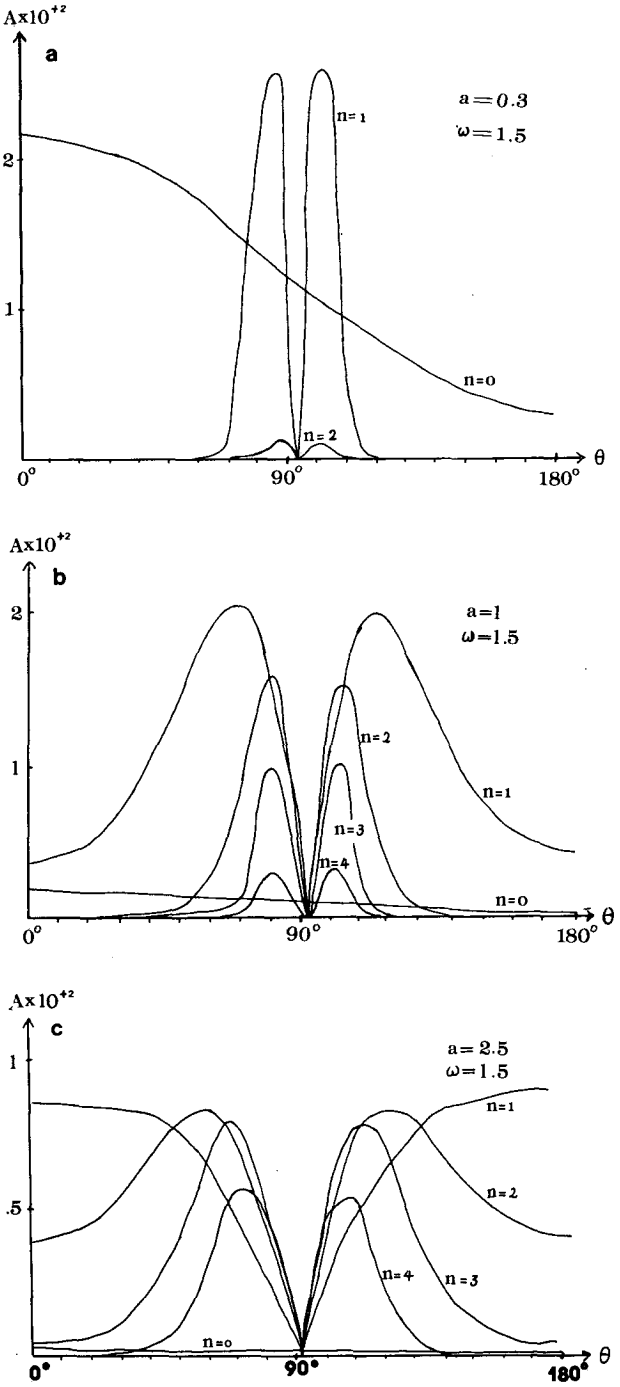

FIG. 6. The relative amplitudes of the barotropic and baroclinic Poincaré waves versus θ for $\omega = 1.5$ and (a) $a = 0.3$, (b) $a = 1$ and (c) $a = 2.5$. The amplitude A is defined in Section 3.

One can see from (47) that the series

$$\sum_{n=1}^{\infty} P_n^w(x,y)G_n(z)$$

converges faster than for the delta-function case,

even as the bump topography approaches the coastline. This is, of course, a consequence of the finite dimension of the bump. The scattering process favors the lowest baroclinic mode, as in the previous case of a delta-function bump. The amplitudes of the diffracted baroclinic Kelvin waves are proportional to the amplitude of the incoming Kelvin wave at $x = x_0$. Thus a bump closer to the shoreline tends to generate larger amplitude Kelvin and Poincaré waves.

4. Numerical estimates

One of the effective generation mechanisms of internal tides is the interaction of the barotropic tide with topographic features having scales of the baroclinic wavelengths (Schott, 1977). The first calculation was done by Munk (1966) applying the bottom slope energy conversion model of Cox and Sandstrom (1962). For the world ocean Munk got 5×10^{11} W. Recently Bell (1975) found an energy flux of 0.9 erg cm^{-2} s^{-1} from barotropic to baroclinic tidal components at the deep ocean rough topography, which amounts to a total of 2.5×10^{11} W for the world ocean. The question as to how much energy flux can be accounted for by the coastal tidal scattering mechanism proposed in this paper will now be addressed.

In order to provide an adequate description of representative bottom topography, some 8000 km of profiles through abyssal hills in the eastern North Pacific were analyzed by Bell (1975). Bell was primarily concerned with internal wave generation by topographic features with scales 0.3 ~ 3 km. At such small scales our coastal wave scattering mechanism may prove irrelevant, and the local generation mechanism is more appropriate. Using the lower wavenumber end of the spectral estimates for abyssal hills topography (from 10–1000 km) obtained by Bell (1975), the rms height of the topography in this band is roughly 125 m, while the average scale of the topography is 50 km. This estimate is subjected to some uncertainty due to the sparsity of data points. The energy flux generated by a bump is not sensitive to the shape of the topography, so that a topographic function of Eq. (43) is used to evaluate the order of magnitude of the baroclinic energy flux. Numerical estimates show that roughly 1.8×10^{-6} of the local M2 energy flux over one average bump is transferred to internal tides. Considering an energy flux of 2.4×10^{11} W and 16000 km coastline from 50°S to 60°N for the M2 tide in the eastern Pacific (Platzman, 1979), we would expect 1.4×10^{8} W of energy flux transferred to internal tide from the eastern boundary of the Pacific. This is equivalent to a 0.09 W energy flux per centimeter of coastline, ~13% of the value (0.7 W cm^{-1}) reported by Schott (1977). Mesoscale bumps of horizontal scale $10^1 \sim 10^3$ km, therefore, is not entirely negligible to the global internal wave budget. Moreover, the mesoscale scattering mechanism may be important for regions with a distinct bump superimposed on a smooth ocean floor, and where the slope conversion model of Sandstrom (1976) is not important.

Recently, Mofjeld and Reed (1978) documented a semidiurnal internal tides propagating seaward from the Washington shelf break. The oscillations were predominately first baroclinic mode, and did not appreciably decay offshore. The mesoscale scattering mechanism is certainly one of the possibilities. However, due to the complicated bathymetry in the vicinity, more observational work further offshore and a better theoretical model including the shelf slope would help to resolve the issue.

5. Conclusions

We have studied the effect of a localized topographic irregularity on the scattering of an incoming barotropic Kelvin wave with a fixed frequency ω. The topographic irregularity is assumed to be small compared to the water depth H, i.e., $h_M/H \ll 1$. An analytical method to decompose the normal modes in the vertical direction is developed. The homogeneous equation (2) with inhomogeneous bottom boundary condition (10) is then transformed into an inhomogeneous governing equation (14) which satisfies the homogeneous bottom boundary condition (12). The problem is then solvable via a Green's function technique employed by Chao and Janowitz (1979).

Notice that Eq. (2) satisfies an inhomogeneous boundary condition [Eq. (10)] at the bottom, while the general solution [Eq. (16)] satisfies a homogeneous boundary condition [Eq. (12)]. This is a consequence of a finite transform (Courant and Hilbert, 1953). In our solution (16), P_z takes a finite jump from $z = 0^+$ to $z = 0$. The solution itself [i.e., $P(x,y,z)$], nevertheless, is continuous across $z = 0^+$. An identical result can be reached if we introduce a function $Y(x,y,z)$ satisfying the inhomogeneous boundary condition, and let

$$P(x,y,z) = Y(x,y,z) + P_H(x,y,z), \qquad (48)$$

where P_H satisfies the homogeneous boundary condition. This method was used by Courant and Hilbert (1953). Substituting (48) into the governing equation (2), it follows

$$\mathbf{L}P_H = -\mathbf{L}Y, \qquad (49)$$

where L is the operator in Eq. (2). Therefore, P_H satisfies an inhomogeneous governing equation. If we decompose (49) into normal modes as we did in Section 2, the same governing equation [i.e., (14)] for P_n immediately follows independent of the func-

tional form of $Y(x,y,z)$ chosen. Therefore, the two methods are equivalent.

For an incoming barotropic Kelvin wave of a super-inertial frequency ($\omega > f$), the diffracted wave fields consist of 1) all baroclinic Kelvin waves in the forward direction, and 2) barotropic and baroclinic Poincaré waves originated at $(x_0, 0)$ and $(-x_0, 0)$, where x_0 is the center of the bump topography. For $\omega < f$, only baroclinic Kelvin waves and some localized disturbance which decays exponentially away from the bump are generated, with higher vertical mode responses trapped nearer to the bump. The scattering process favors the first baroclinic mode for the diffracted Kelvin waves. For $\omega > f$ and a bump size much larger than the baroclinic radius, the barotropic Poincaré wave is the dominant response radiating from the bump topography. As the size of the bump is decreased, higher baroclinic modes become dominant, which is a clear indication that higher modes are localized bottom-trapped responses associated with small topographic irregularities.

The baroclinic Poincaré waves tend to be directionally anisotropic, with higher modes more concentrated in two angular bands centered at $\tilde{\theta} \pm \epsilon$, where $\tilde{\theta}$ is the nodal line and ϵ is a small angle. Apart from the reflection of internal waves from the continental slope as addressed by Rattray (1960) and Sandstrom (1976), etc., the baroclinic Poincaré waves generated by longshore topographic irregularities and radiating offshore in the directions roughly normal to the coastline may contribute significantly to the internal wave field in the open ocean and provide an alternative way to dissipate the tides.

The delta-function solution and a finite-dimension bump are considered. It turns out that the finite dimension of the bump brings about a faster convergence for the normal modes expansion than the delta-function solution. However, a delta-function solution is useful in a sense that, apart from being the fundamental property of Eq. (14), it can be integrated easily to obtain the solution for the case of an extensive bump topography.

The scale for the barotropic Kelvin waves is $R_e \sim 2700$ km, while for a typical ocean, $N'^2 \sim 10^{-5}$ s^{-1}, and the scale for the first baroclinic Kelvin wave is

$$R_i = \frac{N'H}{f} \sim 120 \text{ km}.$$

Therefore, the continental shelf and slope topography, although negligible for the barotropic responses, cannot be neglected as far as the baroclinic responses are concerned. A more realistic model would be to include the continental slope. The dominance of the lower modal responses, as inferred from a linear stratification, appears to be a consequence of the fact that

$$\lambda_0^{1/2} \ll \lambda_1^{1/2} \ll \lambda_2^{1/2} \ll \cdots$$

and is likely to hold for other stratification profiles as well. The solution for an incoming wave other than the barotropic one can also be obtained with relative ease by specifying a baroclinic incoming wave in (9) and in subsequent equations.

A rough numerical estimate shows that ~13% of the observed internal wave energy flux could be due to the mesoscale scattering mechanism discussed in the eastern boundary of the Pacific, and therefore should not be completely neglected in the global internal wave budget. The mechanism could also be of regional importance at places where distinct bumps are superimposed on relatively smooth ocean floors.

Acknowledgments. The author would like to express his thanks to Mr. R. Barbieri, Drs. J. Mueller, P. Schopf and C. McClain of NASA/Goddard Space Flight Center for their administrative help and fruitful discussions, and to Dr. T. W. Kao of The Catholic University and Dr. D-P Wang of The Johns Hopkins University for their valuable suggestions. Thanks are also extended to Drs. F. Schott and H. Mofjeld for furnishing valuable information. The constant encouragement he received from Dr. N. E. Huang of NASA/Wallops Space Flight Center is also acknowledged. Comments from one of the reviewers were helpful. This research was supported by NASA/Goddard Space Flight Center under Contract NAS 5-25811.

References

Baines, P. G., 1974: The generation of an internal tide over steep continental slopes. *Phil. Trans. Roy. Soc. London*, **A277**, 27–58.

Bell, T. H., Jr., 1975: Topographically generated internal waves in the open ocean. *J. Geophys. Res.*, **80**, 320–337.

Buchwald, V. T., 1968: The diffraction of Kelvin waves at a corner. *J. Fluid Mech.*, **31**, 193–205.

Chao, S-Y., and G. S. Janowitz, 1979: The effect of a localized topographic irregularity on the flow of a boundary current along the continental margin. *J. Phys. Oceanogr.*, **9**, 900–910.

——, L. J. Pietrafesa and G. S. Janowitz, 1979: The scattering of continental shelf waves by an isolated topographic irregularity. *J. Phys. Oceanogr.*, **9**, 687–695.

Courant, R., and D. Hilbert, 1953: *Methods of Mathematical Physics*, Vol. 1. Interscience, 560 pp.

Cox, C. S., and H. Sandstrom, 1962: Coupling of surface and internal gravity waves in water of variable depth. *J. Oceanogr. Soc. Japan (20th anniv. ed.)*, **2**, 499–513.

Howe, M. S., and L. A. Mysak, 1973: Scattering of Poincaré waves by an irregular coastline. *J. Fluid Mech.*, **57**, 111–128.

Killworth, P. D., 1978: Coastal upwelling and Kelvin waves with small longshore topography. *J. Phys. Oceanogr.*, **8**, 188–205.

LeBlond, P. H., and L. A. Mysak, 1978: Waves in the ocean. *Elsevier*, 602 pp.

Miles, J. W., 1972: Kelvin waves on oceanic boundaries. *J. Fluid Mech.*, **55**, 113–127.

Mofjeld, H. O., and R. K. Reed, 1978: Semi-daily fluctuations in geopotential off the Washington coast. *J. Mar. Res.*, **36**, 525–528.

Munk, W. H., 1966: Abyssal recipes. *Deep-Sea Res.*, **13**, 707–730.

Mysak, L. A., and C. L. Tang, 1974: Kelvin wave propagation along an irregular coastline. *J. Fluid Mech.*, **64**, 241–261.

Noble, B., 1958: *Methods Based on the Wiener-Hopf Technique*. Pergamon Press, 246 pp.

Packham, B. A., and W. E. Williams, 1968: Diffraction of Kelvin waves at a sharp bend. *J. Fluid Mech.*, **34**, 517–529.

Pinsent, H. G., 1972: Kelvin wave attenuation along nearly straight boundaries. *J. Fluid Mech.*, **53**, 273–286.

Platzman, G. W., 1979: A Kelvin wave in the eastern north Pacific Ocean. *J. Geophys. Res.*, **84**, 2525–2528.

Rattray, M. Jr., 1960: On the coastal generation of internal tides. *Tellus*, **12**, 54–62.

Roseau, M., 1967: Diffraction by a wedge in an anisotropic medium. *Arch. Ration. Mech. Anal.*, **26**, 188–218.

Sandstrom, H., 1976: On topographic generation and coupling of internal waves. *Geophys. Fluid Dyn.*, **7**, 231–270.

Schott, F., 1977: On the energetics of baroclinic tides in the North Atlantic. *Ann. Geophys.*, **33**, 41–62.

Wang, D. P., and C. N. K. Mooers, 1976: Coastal-trapped waves in a continuously stratified ocean. *J. Phys. Oceanogr.*, **6**, 853–863.

Williams, W. E., 1959: Diffraction of an *E*-polarized plane wave by an imperfectly conducting wedge. *Proc. Roy. Soc. London*, **A252**, 376–393.